

Flow-induced bending response rheometer to measure viscoelastic bending of soft microrods

Barrett T Smith,¹ Michał Czerepaniak,² Maciej Lisicki,² and Sara M Hashmi^{1, 3, 4, a)}

¹⁾*Chemical Engineering, Northeastern University*

²⁾*Institute of Theoretical Physics, Faculty of Physics, University of Warsaw, Poland*

³⁾*Mechanical & Industrial Engineering, Northeastern University*

⁴⁾*Chemistry & Chemical Biology, Northeastern University*

(Dated: February 4, 2026)

Soft, microscale hydrogel fibers and rods play important roles in tissue engineering, flexible electronics, soft robotics, drug delivery, sensors, and other applications. Their viscoelastic mechanical properties, while critical for their function, can be challenging to characterize. We present a flow-induced bending response (FIBR) rheometer that quantifies the bending modulus and viscoelastic properties of small, hydrated fibers and rods using flow through a glass capillary. The fiber is positioned across the capillary entrance, and pressure-driven, controlled inflow of water exerts a quantifiable force on the sample. Fiber deflection is determined by video microscopy obtained simultaneously with measurements of flow rate. We develop an analytical model to resolve the hydrodynamic forces applied to the rod, and use Euler-Bernoulli beam theory to determine its material properties. Using a constant volume flow rate of water enables measurement of steady rod deflection, and thus the bending modulus. Application of viscous forces to the rod in a stepwise, cyclic or oscillatory manner enables measurement of time-dependent responses, creep recovery, viscoelastic moduli, and other properties. We demonstrate the versatility of this technique on natural and synthetic materials spanning diameters from 1 to 500 microns and elastic moduli ranging from 100 Pa to >100 MPa. Because the technique uses water to exert forces on the fiber, it works particularly well for hydrated materials, such as hydrogels and biological fibers, providing a versatile platform to characterize microscale mechanical properties of elongated structures.

^{a)}s.hashmi@northeastern.edu

I. INTRODUCTION

Soft, microscale, hydrogel fibers and small rods ($< 200 \mu\text{m}$ in diameter) play important roles in tissue engineering, flexible electronics, soft robotics, drug delivery, sensors, and many other applications¹⁻⁴. Their viscoelastic mechanical properties are critical for their function, but characterizing these properties can be challenging. Bulk and macroscale testing, such as shear rheology or traditional dynamic mechanical analysis techniques, is often unfeasible for small, soft, fibrous materials as they are often too small to load into macroscale equipment. Further, particularly soft samples may be too soft to be effectively clamped into place, as the clamping force may damage the material. Additionally, biological samples and hydrogels have different properties in wet and dry environments. These limitations necessitate alternative techniques that can probe microscale materials, especially in their hydrated state.

Atomic force microscopy (AFM) with Force Spectroscopy Mapping is a well-established and widely used nanoindentation method for determining the mechanical properties of small, soft materials^{5,6}. The ability to perform and accurately interpret AFM experiments depends on the probe shape, size, and sample interactions. The probe size and shape are critical to the success of the measurement, and each requires separate mathematical models to correctly interpret the results. Probe geometry determines the amount and nature of the contact between the probe and sample surface. Therefore, different probe shapes experience different adhesion forces and varying degrees of interference from the underlying substrate⁷⁻¹⁰. Larger probes match the bulk properties more precisely but are more prone to substrate interference¹¹. Smaller probes show more variability over the material surface, particularly for porous materials such as hydrogels^{11,12}. As a result, bulk material properties do not always match localized AFM measurements^{11,13,14}. In addition to probe-related considerations, the aqueous environment required by most hydrogels and biological samples adds further complications. Surface tension complicates measurements, particularly for soft materials, where the forces involved are of a similar magnitude to the surface tension^{15,16}. Friction and adhesion issues are also more pronounced in water^{17,18}. This can make it difficult to find the material surface and add to the complexity of the analysis. While AFM can provide reasonable mechanical measurements of soft materials when experiments are carefully designed and controlled, its complexity is nontrivial and motivates the development of

alternative, simpler, and more accessible approaches.

Beyond AFM, many techniques have been developed for characterizing the material properties of small, soft materials¹⁹. Optical tweezers can probe very small hydrated samples to determine their viscoelastic mechanical properties. However, the generated forces may be insufficient for stiffer samples, and samples must be transparent^{20,21}. Another approach involves fixing one or both ends of a fiber in place and using gravity or fluid flow to induce bending while measuring the resulting deformation²²⁻²⁴. However, the required sample configuration is not feasible for all sample types. Capillary aspiration techniques provide an alternative by using glass capillaries that form a seal on the material surface, with an applied vacuum causing measurable deformation²⁵⁻²⁷. In capillary micromechanics, materials suspended in pressure-driven flows are immobilized at the tapered end of a capillary. Deformation as a function of applied stress provides mechanical property measurements²⁷. Both capillary aspiration and capillary micromechanics techniques are frequently used on spherical samples. Achieving a tight seal may be difficult for especially porous or irregular surfaces, resulting in errors in measurement or difficulty in generalizing the mechanical properties of a small piece of the surface to an entire material. A related approach eliminates the need for a seal by relying instead on fluid flow past the sample to exert the deforming force, although this technique has only been demonstrated to measure the elastic modulus of diatom colonies²⁸. Further validation and theoretical development is needed to establish and expand this method.

To address the shortcomings of available bulk and microscale characterization techniques, we propose a flow-induced bending response (FIBR) rheometer to determine the bending modulus and viscoelastic properties of small hydrated fibers and rods using flow through a glass capillary. The technique positions the fiber perpendicular to the capillary. The flow of water into the capillary exerts quantifiable forces on the sample, and microscopy measures the fiber deflection to determine the material moduli. The method is simple and uses common readily available equipment. It works well for fibers, both natural and synthetic, with diameters between 1 and 500 μm . We measure materials with elastic moduli ranging over nearly 7 orders of magnitude in stiffness, from 100 Pa to >100 MPa. Because the technique uses water to exert force on the fiber, it works particularly well for hydrated materials, such as hydrogels and biological fibers. We develop a theoretical analytical framework that accounts for hydrodynamic interactions between the fiber and the fluid flow to calculate

the force exerted on the fiber. Then we use Euler-Bernoulli bending theory to determine the bending modulus as a function of the applied force and measured fiber deflection. Here we provide a detailed validation of the FIBR rheometer and show its ability to go beyond elastic measurements to measure time-dependent and viscoelastic material properties as well as investigating failure.

II. MATERIALS AND METHODS

A. Materials

Sterilized downy duck feathers are taken from a couch pillow (Pacific Coast Feather Cushion, North Carolina USA). The barbules are stripped from the barbs via tweezers. Polyester fibers are obtained from the mouthpiece plug of a VWR Disposable Serological Pipet and used without further modification.

Sodium alginate, magnesium chloride, and sodium chloride are obtained from Sigma-Aldrich. Calcium chloride is obtained from VWR. All chemicals are used as received. Solutions of sodium alginate, calcium chloride, magnesium chloride, and sodium chloride are prepared in DI water (Milli-Q Advantage A10). Concentration details are provided in the following sections.

Glass capillaries with internal diameters of 200, 600, 1000, or 2000 μm are purchased from VitroCom and World Precision Instruments (WPI) and are connected to pump tubing via a capillary holder (WPI MPH3) or, for capillaries that do not fit in the holder, are attached directly to the pump tubing using epoxy.

B. Alginate Fiber Manufacture

Alginate fibers are generated by extrusion through a blunt needle into a calcium bath^{29,30}. Sodium alginate is dissolved in water at a concentration of 2% by weight. A syringe pump pushes 0.5 mL of the alginate solution through a 34 gauge blunt needle at 30 mL/hr into a bath of calcium chloride (2% in water). The alginate fibers form instantly, although gelation continues for at least 24 hr before any measurements to allow for the complete diffusion of calcium through the fiber. The fibers produced by this method have diameters between 125 and 250 μm .

To significantly change the mechanical properties of the alginate fibers, we use magnesium as an alternate crosslinker or include sodium chloride in the ion bath, as both are known to soften alginate gels^{31,32}. However, direct extrusion into a magnesium bath does not produce fibers; only calcium chloride at specific weight percents (1-4%) allows for the formation of fibers. Therefore, the fibers are removed from the calcium bath with tweezers immediately after extrusion and placed into a bath with alternate salts: either a 2% solution of magnesium chloride or a solution with 2% calcium chloride and 1% sodium chloride. While some calcium carries over with the newly formed alginate fibers, we transfer only approximately 0.1 g of fiber into a 10 mL bath, so that the calcium concentration is reduced by at least a factor of 100. Fibers are allowed to equilibrate in the new ion solution for at least 72 hr before measurement. Fibers placed in the magnesium bath swell slightly for a final diameter of 200–300 μm . Fibers cross-linked in a calcium bath are referred to as Ca-alginate fibers, while those transferred to the magnesium bath are Mg-alginate fibers.

C. Alginate Rod Manufacture

Alginate rods are generated in a microfluidic device^{33,34}. The device consists of a Y-shaped intersection. All channels are 40 μm wide and 25 μm tall. A pressure controller (Fluigent LU-FEZ) with an attached flow-rate meter is used to control flow rates. A solution of fluorescently-tagged sodium alginate (0.1 mg/mL) flows at 1 $\mu\text{L}/\text{min}$ in one inlet and meets a solution of calcium chloride (100 mM) also flowing at 1 $\mu\text{L}/\text{min}$. Sodium chloride is present in both streams at 2.5 mM. Where the two inlet streams meet at the Y-intersection, gel deposits on the channel wall. The gel grows to fill the cross-section of the channel for up to 1 mm downstream of the junction. The deposited gel occludes the channel, requiring higher driving pressures to maintain the set flow rate. At a certain threshold, shear stresses from the fluid are sufficient to remove the gel from the channel wall and flush it out of the device. The eluted gel keeps the form of the channel, resulting in a rod 500-1000 μm long with a 25 \times 40 μm rectangular cross-section. Alginate rods are kept in the elutant until measured.

D. Rheology

Bulk alginate gels are made according to an established method³⁵. Sodium alginate solution (2% in water) is added to a 3D printed circular mold (50 mm in diameter). Filter paper (Whatman no. 1) impregnated with 2% calcium chloride solution is placed atop the alginate solution and secured in place with another 3D printed part. Several milliliters of a solution of the desired divalent cation is placed on top of the filter and allowed to diffuse into the alginate solution. After at least one hour, the gel can be removed from the mold, the filter stripped from the gel, and the gel placed in a larger volume of the desired ion solution, either 2% calcium chloride or 4% magnesium chloride. Gelation is allowed to continue for at least one day. After the alginate has completely gelled, the sample is trimmed to the size of the rheometer geometry.

Prepared gels are added to a 40 mm plate-plate geometry for small angle oscillatory shear (SAOS) measurements consisting of an frequency sweep followed by an amplitude sweep. The amplitude sweep is measured at an angular frequency $\omega = 5$ rad/s. All samples exhibit a linear regime with constant modulus at strains below 0.1%. The frequency sweep is measured at an oscillatory strain of 0.1%, which is within the linear regime found from the amplitude sweep for all samples.

E. Capillary Aspiration

Glass capillaries with internal diameters of 0.2 – 2 mm are secured into the tubing of a pressure controller with an associated flow rate meter (Fluigent LineUp Push-Pull). The pump can operate between –0.9 bar and 1 bar. A custom designed 3D-printed well (4 mL capacity) is affixed to a glass slide using epoxy. The capillary is positioned using a micromanipulator (WPI) over the objective of an inverted microscope (Leica DMIL). The entire setup is mounted on an air table (Thorlabs) to minimize vibrations. A schematic of the experimental setup is provided in Figure 1.

The glass slide well is filled with water before adding a sample. The sample position is manipulated using the microscope stage and/or tweezers until the rod is positioned transversely to the capillary opening. A small negative pressure draws water into the capillary, holding the rod in position before the flow tests begin. This corresponds to 50-500 μ L/min.

The required flow rate depends on fiber and capillary size. To maintain a constant volume of water in the slide well during all measurements, a separate pump supplies water to the well at a flow rate equal to that being removed through the capillary.

Once the rod is positioned, flow tests are conducted. We control applied pressure and record flow rate Q through the Fluigent software for the duration of the experiment. We perform three different types of flow tests: elastic measurements, creep measurements, and dynamic mechanical analysis (DMA). For each, the increment size and maximum applied vacuum depend on the sample's effective stiffness. The appropriate applied pressure for any sample is not known *a priori*, but is determined via experimentation. The achievable flow rates depends on the size of the capillary. For the small 200 μm capillary, flow rates vary between 0 – 1000 $\mu\text{L}/\text{min}$, while for the large 2000 μm capillary, achievable flow rates exceed 12000 $\mu\text{L}/\text{min}$.

For measurements of elastic materials, vacuum is applied in regular increments. At least several seconds elapse between each increment to allow the sample to reach steady-state deflection. For creep measurements, a large step change in flow rate is applied and held for more than 60 s while deflection is measured. Afterwards, flow rate is dropped to a baseline of sufficient magnitude to prevent the fiber from falling off the capillary. For DMA measurements, flow rate is varied in a sinusoidal pattern with a period of 10 s.

F. Microscopy and Video Analysis

We record fiber deflection δ using a bright field inverted microscope (Leica DMIL) at either 10 \times or 20 \times magnification, at a spatial resolution of 0.77 and 1.53 pixels/ μm respectively. The microfluidic alginate rods are imaged using fluorescent microscopy, as they contain a fluorescein labeled alginate. The timestamp from each video frame is matched to the corresponding flow rate data to determine the deflection δ and flow rate Q for each frame.

Each video frame is analyzed to determine the position of the rod or fiber edge using the steps indicated in Figure 1b. First, images are cropped to focus on the rod edge positioned in the center of the capillary where we expect the most deflection. The grayscale images are then binarized. For samples that are transparent or for which binarization does not reveal the rod edge, Python Skimage filters (Sobel or Sato) are used to illuminate the edges

before binarization³⁶. Having successfully isolated the rod edges, we find all contours in the image and sort them by x -position to determine the right and left edges of the rod. Finally, a 10th order polynomial, sufficient to capture any irregularities in the rod edge, is fitted to the contour for use when comparing across frames. After identifying a baseline frame, polynomial fits from each frame are compared to the baseline at each x -position to find the greatest distance between the edges. This distance is the deflection of the rod δ .

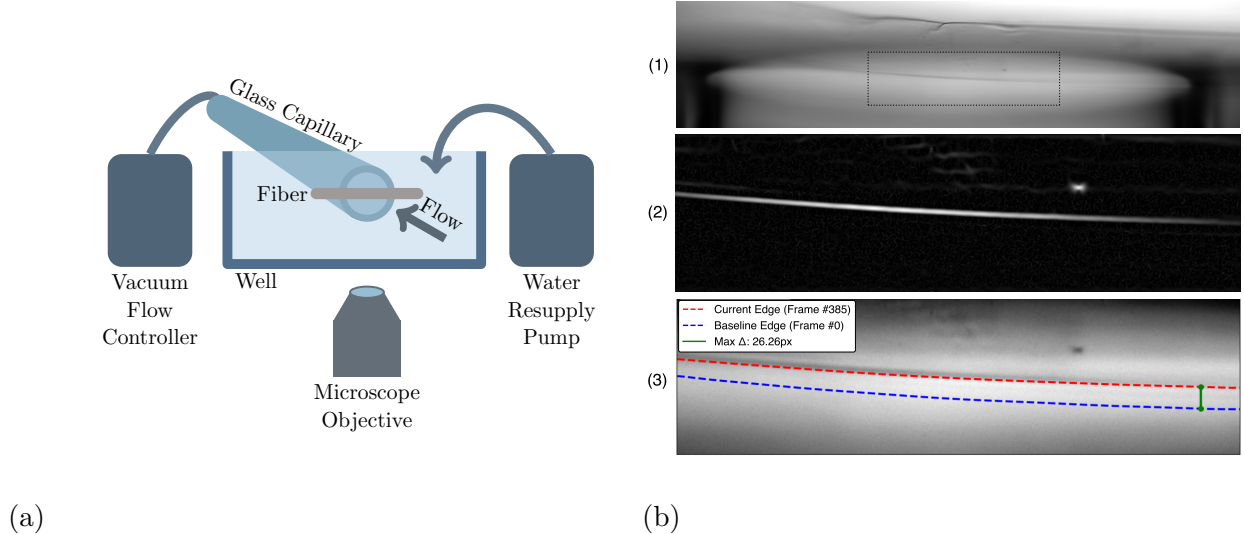


Figure 1: (a) Schematic of the experimental setup. (b) Image analysis pipeline: (1) Raw microscope image with a dotted box to represent the crop used in the analysis, (2) The cropped image with an applied Sato filter, (3) Polynomial fit of the contour found in the Sato filter and comparison of this polynomial, in red, to the baseline, zero-deflection frame, in blue.

III. THEORY

The fluid drag forces that act on a fiber placed in an external flow induce a deformation, the shape of which results from the balance between elastic and hydrodynamic stresses. Given the microscale sizes, the flow around the fiber is governed by the Stokes equations. To resolve the hydrodynamic forces, we construct a bead model and use the mobility matrix formalism. The details of the calculation are included in the SI. We approximate hydrodynamic interactions between the subunits of the fiber with the Rotne-Prager-Yamakawa tensor^{37–39}. This approach enables us to relate the local drag acting on the filament to the

imposed velocity distribution at the entrance to the capillary tube. These forces are then used to model the deflection using a continuous Euler-Bernoulli beam equation⁴⁰. We assume that the deformation of the fiber is sufficiently small such that the change in shape does not affect the form of the mobility matrix.

The capillary entrance flow interpolates between a quiescent fluid far away from the orifice and a fully developed Hagen-Poiseiulle flow inside the capillary⁴¹. To reflect this fact, we assume that the axisymmetric flow profile at the location of the fiber has a quartic dependence on the distance from the axis

$$U_{\text{ext}} = U_{\text{max}} \left[1 - \left(\frac{r}{R} \right)^4 \right], \quad (1)$$

where r is the distance from the axis and R is the radius of the capillary, and that the presence of the fiber does not disturb this flow. The velocity field is related to the imposed volumetric flow rate inside the capillary

$$Q = \int U_{\text{ext}} \, dS = \int_0^{2\pi} \int_0^R U_{\text{max}} \left(1 - \frac{r^4}{R^4} \right) r \, dr \, d\phi = \frac{2}{3} \pi R^2 U_{\text{max}}. \quad (2)$$

To introduce elastic stresses, we discretize the fiber into beads of radius a (and diameter d) each, with the distance l_0 between their centers. Next, we assume that the associated profile of the drag force density f (force per unit length) has a shape that is qualitatively similar to that of the flow,

$$f = \frac{F_{\text{max}}}{l_0} \left[1 - \left(\frac{r}{R} \right)^4 \right], \quad (3)$$

where l_0 is the distance between the centers of the neighboring beads. Both force and velocity profiles are sketched in Figure 2a. We expect this assumption to hold in the central part of the fiber, close to the axis of the capillary. This assumption can be justified using arguments analogous to classical resistive force theory, where the relationship between the velocity and force density remains a purely local quantity⁴².

Once the magnitude of the force is known, the maximal deflection of a deformed fiber that is accessible in experiments can be found from solving the Euler-Bernoulli elastic beam problem in the limit of small deflections. Parameterizing the shape of the fiber by its arclength s , the vertical deflection $z(s)$ satisfies

$$EI \frac{d^4 z}{ds^4} = - \frac{F_{\text{max}}}{l_0} \left(1 - \frac{s^4}{R^4} \right) \quad (4)$$

with E being the Young's modulus, and I being the second moment of cross-sectional area of the fiber. We solve this equation with the boundary conditions of the fiber being simply supported at the walls of the capillary, which means that its vertical position is fixed there, and the ends are torque-free, so that

$$z(\pm R) = 0 = z''(\pm R). \quad (5)$$

We note that when choosing such boundary conditions we neglect the influence of the remaining part of the fiber, outside of the capillary, on the overall shape of the fiber. However, we postulate that these parts would not dramatically influence the shape of the beam in the central part of the capillary.

Integration of Eq. (4) with the boundary conditions (5) leads to the following relationship between the maximal deflection δ and the Young's modulus

$$EI\delta = \frac{f_{\max}R^4}{5}, \quad (6)$$

with $f_{\max} = F_{\max}/l_0$ being the maximal force per unit length of the fiber.

To relate the maximal force per unit length to the imposed velocity amplitude U_{\max} , we must consider hydrodynamic interactions within the fiber. To do so, we analyze the hydrodynamic drag on the mid-point of the fiber under a known distribution of hydrodynamic forces that results from the fiber being placed in an external flow. The details of this calculation rely on the mobility matrix formalism and are described in the SI. Here, we present the final result.

We distinguish two cases, depending on the fiber thickness d in comparison to the radius of the capillary R . We define 'thick' fibers as ones with a diameter greater than the radius of the capillary, while 'thin' corresponds to an increasing aspect ratio $k = R/d$. The distinction between the modeling approaches for these two fiber regimes is illustrated in Figures 2b and 2c. For thin fibers, we find that

$$f_{\max} \approx U_{\max} \frac{4\pi\eta}{\log k + 1.86}. \quad (7)$$

It is worth noting that the result is very close to that obtained using resistive force theory^{42–44}; it differs only by an additive term in the denominator, which becomes negligible for sufficiently large length-to-thickness ratios. This result is approximate, as it is based on the assumption of a sufficiently large aspect ratio. Nevertheless, the deviation

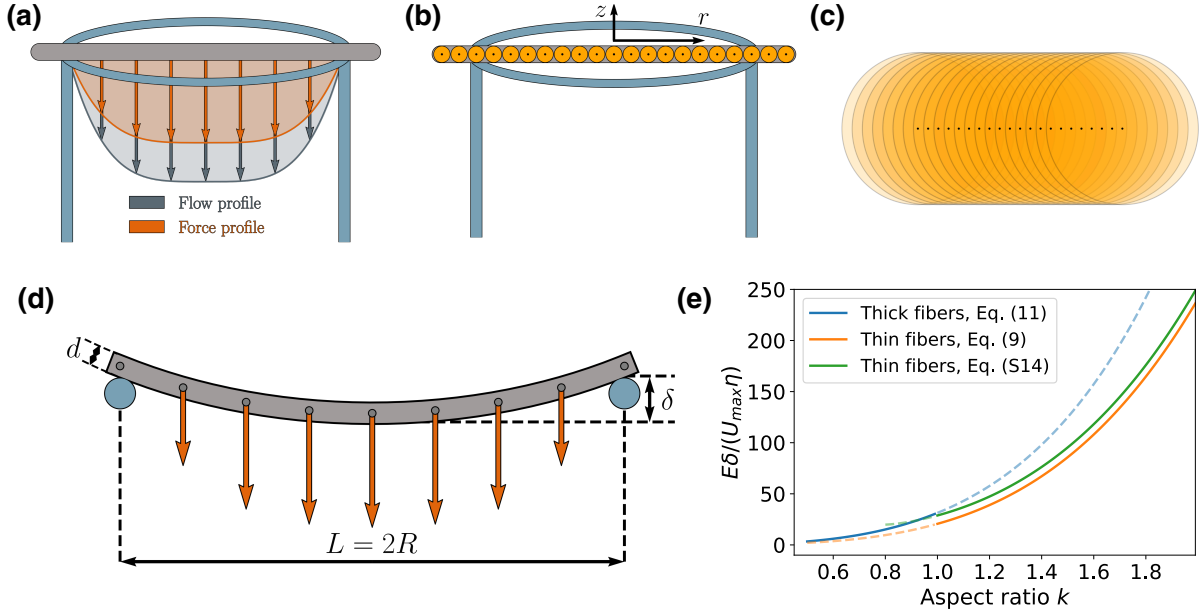


Figure 2: (a) Schematic illustration of a fiber (grey) placed inside a capillary tube, showing the flow velocity profile, Eq. (1), and the force profile acting on the fiber, Eq. (3). (b) A continuous “thin” fiber is discretized as a collection of mutually connected beads, each pair of neighboring beads being in point contact. This approach allows the computation of hydrodynamic forces acting on the fiber using Eq. (S8). (c) A continuous “thick” fiber is discretized as a set of overlapping, connected beads. This approach allows the computation of hydrodynamic forces acting on the fiber using Eq. (S12). (d) Schematic illustration of a deformed fiber: the capillary tube has radius R , the fiber has thickness d , and the deflection is denoted by δ . The distribution of hydrodynamic forces acting on the fiber is also sketched. (e) Plot of the dimensionless Young’s modulus $E\delta/(U_{max}\eta)$, as a function of the ratio of the tube radius to the fiber thickness, $k = R/d$, for ‘thin’ fibers (Eq. (9)) in orange and ‘thick’ fibers (Eq. (11)) in blue. The dashed lines indicate the continuation of the relationship, extrapolated into regimes where it is no longer valid (e.g., the ‘thick’ regime extended into the ‘thin’ regime). The modulus plotted in green represents the exact expression (Eq. (S14)) for thin fibers, relaxing the assumption of large aspect ratio k .

from the result obtained without this assumption (Eq. (S10)) is small. For thick fibers, the resulting expression is

$$f_{max} = U_{max} \frac{3\pi\eta}{\frac{R}{d} \left(\frac{8}{5} - \frac{3}{8} \frac{R}{d} \right)} \quad (8)$$

Because the hydrodynamic force scales with velocity, the force profile along the length of the fiber has the same shape as the flow profile, as illustrated in Figure 2d.

Combining the results above, we find the expressions for the Young's modulus of the fibers. For a thin fiber with a cylindrical cross-section, with $I = \pi a^4/4$, and aspect ratio k , we have

$$E = \frac{192}{5} \frac{U_{\max} \eta}{\delta} \frac{k^4}{\log k + 1.86}, \quad (9)$$

For non-circular cross-sections, the bead model remains the same, but the moment of interia changes. For instance, for a rod with a square cross-section, $d \times d$ and $I = d^4/12$, we find

$$E = \frac{36\pi}{5} \frac{U_{\max} \eta}{\delta} \frac{k^4}{\log k + 1.86} \quad (10)$$

For a thick cylindrical fiber, the logarithmic term is replaced and the expression reads

$$E = \frac{\eta U_{\max}}{\delta} \frac{24k^3}{1 - \frac{15}{64}k}, \quad (11)$$

while for a thick square cross-section,

$$E = \frac{\eta U_{\max}}{\delta} \frac{18\pi k^3}{4 \left(1 - \frac{15}{64}k\right)}. \quad (12)$$

The final expressions above can be used to directly predict the Young's modulus given the measured deflection of the fiber δ and its thickness d , as well as the size of the capillary used for the measurement. Figure 2e plots $E(k)$ for thin (Eq. (9)) and thick (Eq. (11)) fibers, along with the exact solution for thin fibers, relaxing the assumption of large k (Eq. (S14)).

In all the cases considered, the Young's modulus is proportional to the ratio of maximal flow velocity to maximal deflection, and can be written as

$$E = B(R, d) \frac{\eta Q}{\delta}, \quad (13)$$

where $B(R, d)$ is a geometric parameter, and the measured quantity Q is derived from U_{\max} using Eq. (2). These expressions serve as the basis for the analysis and interpretation of experimental data throughout this work.

IV. EXPERIMENTAL RESULTS

A. Behavior of elastic materials in the capillary bending assay

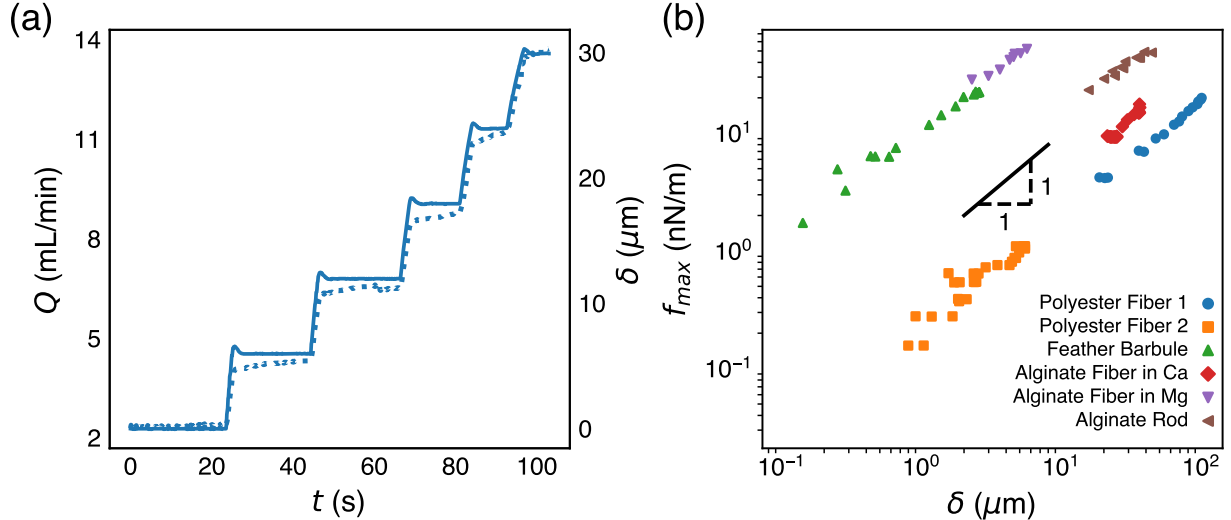


Figure 3: (a) Elastic behavior of a polyester fiber. The solid line shows the flow rate of water pulled into the capillary, while the dotted line shows the deflection of the fiber. (b) Elastic behavior in a range of materials, where the polyester fiber from (a) is in blue.

Figure 3a shows the raw data for a polyester fiber bent via capillary aspiration on a 2000 μm capillary. The plot shows the volumetric flow rate Q (left axis, solid blue line) and the fiber deflection δ (right axis, dotted orange line) as functions of time. The experiment starts at a flow rate of ~ 2 mL/min which exerts a force sufficient to hold the fiber in place and prevent the fiber from falling from the center of the capillary. In the experiment, flow rate increases stepwise by 2 mL/min every ~ 20 s. The delay in changing flow rates ensures that the fiber reaches an equilibrium position at each new flow rate. With each increase in flow rate, the fiber deflection increases a proportional amount, ~ 6 additional micrometers for each 2 mL/min increase in flow rate.

Figure 3b shows measurements of deflection δ of several materials as a function of the force per unit length applied by the fluid flow. Each data point represents a deflection similar to that seen in the plateaus in Figure 3a. We use Equation 7 coupled with Equation 2 to calculate f_{max} from measurements of Q . The plot is on log-log axes to demonstrate the wide range of possible exerted forces (0.1 – 100 nN) and measured deflections (0.1 – 100 μm). The

materials cover a range of synthetic and bio-materials. Each material shows linear behavior, as indicated by a slope of 1 on the log-log plot. The polyester fiber in Figure 3a is shown in blue in Figure 3b.

The linear relationship between f_{\max} and δ suggests an elastic material response. Eq. (6) shows that $f_{\max} \sim \delta EI/R^4$. The slope of each measurement of $f_{\max}(\delta)$ is proportional to the effective stiffness of the sample, EI . Along with the sample dimensions, the slope can be used to determine the intrinsic elastic modulus of the material.

We can see the effect of capillary size when comparing the two polyester fiber traces. Polyester fiber 1 (in blue) was measured on a capillary with $2R = 2000 \mu\text{m}$, while polyester fiber 2 (orange) was measured on a capillary with $2R = 600 \mu\text{m}$ capillary. Both fibers are $28 \mu\text{m}$ in diameter. The achievable flow rates and forces are lower on the smaller capillary, and the resulting deflections are much smaller. Nevertheless, they share a line on the plot, indicating a similar effective stiffness. Therefore, since the two samples are the same size, with the same I , they share a similar modulus.

Using Eq. (6) we convert the slopes of the data shown in Figure 3b to measurements of E . Table I shows several biological and synthetic materials measured using this capillary aspiration technique. The effective stiffness of the materials range over 6 orders of magnitude from 10^{-18} to 10^{-12} Pa m^4 . The moduli also vary by more than six orders of magnitude from 10^2 to 10^8 Pa .

Down feathers are widely used in clothing and upholstery, and their mechanical properties are well-characterized⁴⁵⁻⁴⁸. Feathers contain a central spine called a rachis, from which branch regularly spaced fibers known as barbs with diameters of $\sim 20 \mu\text{m}$. Branching from the barbs are much smaller fibers called barbules, typically $\sim 2 \mu\text{m}$ in diameter and $< 0.5 \text{ mm}$ in length. Barbs are sufficiently large to be measured using macroscale techniques and have Young's moduli ranging from $0.5 - 2.5 \text{ GPa}$. A $20 \mu\text{m}$ feather barb with an elastic modulus of 2 GPa will have an effective stiffness $EI > 10^{-11}$, which is too stiff for this technique. Feather barbules are too small for macroscale characterization, but share a chemical composition with the barbules. The smaller diameter of the feather barbules significantly lowers the effective stiffness so that they can be measured on the capillary. As measured on a $200 \mu\text{m}$ capillary, the feather barbules have a bending modulus of 201 MPa . To the best of our knowledge, this is the first mechanical measurement of a feather barbule. The measured modulus is lower than that of feather barbs. Beyond the difference

Material	n	EI (Pa m ⁴)	E (Pa)	Modulus from other technique (Pa)
Downy feather barbule	3	$7.82 \pm 1.08 \times 10^{-18}$	$2.01 \pm 0.13 \times 10^8$	$E = 0.5 - 2.5 \times 10^9$, Ref. ⁴⁵⁻⁴⁸
Polyester Fiber	4	$1.44 \pm 0.23 \times 10^{-12}$	$4.94 \pm 0.58 \times 10^7$	$E = 1 - 10 \times 10^9$, Ref. ^{49,50}
Ca-alginate Fiber (2%:2%)	4	$4.51 \pm 2.91 \times 10^{-12}$	$1.82 \pm 0.82 \times 10^4$	$G' = 5.0 \times 10^3$ (SAOS)
Ca-alginate Fiber (2%:2%) + 1%NaCl	5	$5.2 \pm 2.23 \times 10^{-12}$	$1.30 \pm 0.25 \times 10^4$	—
Mg-alginate Fiber (2%:2%)	8	$3.14 \pm 2.35 \times 10^{-14}$	$3.02 \pm 2.52 \times 10^2$	$G' = 129$ (SAOS)
Alginate Rods	5	$1.19 \pm 1.05 \times 10^{-15}$	$4.40 \pm 3.61 \times 10^4$	$E = 7 \times 10^3$ (AFM)

Table I: The effective stiffnesses and elastic moduli for many materials as tested via capillary aspiration. Also, elastic or shear moduli for similar materials via other techniques.

in materials (barb versus barbule), one reason for this difference may be the hydration of the barbule. The elastic moduli of feather barbs is reduced by nearly half when wet^{46,48}.

Polyesters are synthetic polymer materials that are used in a wide range of applications. The elastic modulus varies significantly based on the crystallinity and fiber alignment within the sample, but is generally between 1 and 10 GPa⁴⁹⁻⁵¹. The polyester fiber modulus measured via capillary aspiration, either with a 600 μ m or 2000 μ m capillary as shown in Figure 3b, is significantly lower than that expected at 49.4 MPa. There are several possible explanations for this observation. First, similar to the feather barbule, the elastic modulus is significantly lower when the fibers are submerged in water⁵⁰. Second, polyester fibers may be hollow, changing the moment of inertia I and skewing the elastic modulus calculation⁵².

Alginate is a biopolymer extracted from sea algae used in food, cosmetics, and pharmaceuticals. Multivalent cations crosslink the polymer chains to form a gel. Alginate gels in

the bulk have been widely studied and vary in their mechanical properties based on the specific composition and molecular weight of alginate and the species and concentration of the cross-linker. The modulus of bulk calcium alginate gels can vary from 1 to >100 kPa^{32,53,54}. Magnesium alginate gels are much softer, with elastic moduli ranging from 0.07–1.8 kPa³¹. Beyond changing the cross-linking ion, the moduli of alginate gels can be lowered by the addition of monovalent cations such as sodium³². Differences in manufacturing processes also impact the resulting gel, with factors like molecular fiber alignment and post-gelation drying impacting the elastic modulus^{55,56}. Because of the wide variation in material properties, we perform small-amplitude oscillatory shear (SAOS) tests on bulk gels formed with either calcium (Ca-alginate) or magnesium (Mg-alginate) as the cross-linkers. When measured via SAOS, the Ca-alginate and Mg-alginate gels have storage moduli G' of 5040 Pa and 124 Pa, respectively (see Figure S2). These are well within the range of moduli found in the literature.

Table I lists the bending results for the three different compositions of alginate fibers measured on 600, 1000, or 2000 μm capillaries. Calcium alginate fibers have a measured elastic modulus of 18.2 kPa. The modulus decreases by $\sim 30\%$ to 13.0 kPa when sodium chloride is added to the calcium ion bath. Using Mg as the cross-linking agent results in the weakest fibers, with an elastic modulus of only 300 Pa. Because fibers formed via bath extrusion are likely isotropic and homogeneous⁵⁵, we can relate the bending modulus of the fibers found by the FIBR rheometer to the elastic modulus of the bulk gels determined via SAOS. To compare the results from the rheometer and capillary bending, we must consider that the Young's modulus and storage component of the shear modulus are not the same measurement. Instead, for isotropic materials with a Poisson's ratio of 0.5 and bulk modulus $B \gg E$, the relationship between the elastic modulus E and shear modulus G' is $E = 3G'$ ^{57,58}. For both the Ca-alginate and the Mg-alginate fibers, the moduli measured by the FIBR rheometer are indeed $\sim 3\times$ the storage moduli values of the bulk alginate gels as determined by SAOS. Thus, we see excellent agreement between the two separate measurement techniques.

Finally, we measure alginate rods produced in a microfluidic device. These rods are unique in several respects. They form at concentrations of alginate much lower than is possible by the direct extrusion method used above (0.01 % versus 2 %). The rods are formed during microfluidic flow, while cross-linking in the extruded fibers occurs only after the algi-

nate flows through the needle, so that their internal structure is isotropic. Additionally, the alginate rods are microporous, whereas the extruded fibers are uniform. Because of their small size, $25 \times 40 \mu\text{m}$ in cross-section and less than 1mm in length, bulk scale characterization is not possible. As shown in Table I, the alginate rods are substantially stiffer than the alginate fibers at $E = 44 \text{ kPa}$ as measured on a $200 \mu\text{m}$ capillary. Interestingly, the alginate rods are softer when measured via AFM at 7 kPa . This is likely due to flow-induced internal fiber alignment within the alginate rods, which causes anisotropy in the material. In a different context, alginate fibers made by electrospinning causes fiber alignment, also inducing anisotropic structure, as confirmed by small angle X-ray scattering⁵⁵. The anisotropic fibers have higher elastic moduli than their isotropic counterparts.

B. Non-elastic behavior

For many materials, an elastic modulus is sufficient to characterize the mechanical response. However, for viscoelastic materials, the FIBR rheometer can also characterize the time-dependent viscous response, either via creep measurements or Dynamic Mechanical Analysis techniques. We also explore fiber failure.

1. Creep

Figure 4 shows the creep behavior of the different alginate fibers. Creep refers to the time-dependent movement of a material upon application of a steady force. Figure 4a shows the raw flow rate (black) and deflection data (colored by time) for the Ca-alginate fiber creep measurements on a 1mm capillary. At $t = 30, 160$ and 280 s , flow rate is increased and held steady for at least 60 s to apply a constant force. Afterwards, the flow rate is dropped to a low value. At each application of force the fiber reaches an equilibrium deflection within several seconds. Upon removal of the force, the fiber recovers its original baseline deflection within 30 s.

Figure 4c shows a similar experiment for a Mg-alginate fiber measured on a 0.6 mm capillary. Because the Mg-alginate fiber is much less stiff, it deflects a similar amount on a smaller capillary and at lower flow rates than the Ca-alginate fiber measured on the 1 mm capillary in Figure 4a. At each application of force, the Mg-alginate fiber in Figure 4c shows

an initial $1.5 \mu\text{m}$ jump in deflection, followed by a linear increase in deflection, while the force is maintained. Upon releasing the force, the deflection drops an amount similar to the initial increase, but does not recover from the slower, linear deformation. As a result, there is a net increase in fiber deflection over the course of the creep cycles.

Figures 4b and 4d show the creep data from Figures 4a and 4c, respectively, as well as the fit of the Burgers model of viscoelasticity^{59,60}. The color of each curve in Figures 4b and 4d corresponds to the same colored cycle in Figures 4a and 4c. The Burgers model consists of a Kelvin-Voigt element, a damper and spring in parallel, in series with a Maxwell element, a damper and spring in series. The viscoelastic compliance J of a Burgers material behaves according to:

$$J(t) = \frac{\gamma(t)}{\sigma_0} = \frac{1}{G_0} + \frac{1}{G_1} (1 - e^{-t/\tau}) + \frac{t}{\eta}$$

where G_0 and G_1 are the shear moduli of the spring elements in the model, τ is the decay time, and η is the material viscosity. To calculate the viscoelastic compliance $J(t)$, we determine strain in the rod $\gamma(t)$ from the deflection: $\gamma(t) = 6\delta d/4R^2$, and stress in the rod σ_0 from the force: $\sigma_0 = 3FR/\pi 4d^3$, using three-point flexural analysis based on the Euler Bernoulli beam bending theory. For the purpose of fitting the model, each creep cycle is processed independently. The deflection at the start of each creep measurement is subtracted from all deflection values during that creep cycle so that the deflection starts at 0 for fitting. After fitting the model to this offset data, the initial deflection is added back to the fitted curves to generate the plots in Figures 4b and 4d .

Comparing the fit parameters found in Figures 4b and 4d between the Ca-alginate and Mg-alginate fibers shows dramatic differences. The instantaneous elastic response G_0 for the Ca-alginate fiber is approximately 100 times larger than G_0 for the Mg-alginate fiber, similar to the difference seen in the elastic moduli found in Table I. This makes sense as the Ca-alginate fiber shows a similar magnitude deflection despite experiencing much faster flow, and consequently higher forces, on a larger capillary. The materials have similar Kelvin-Voigt elements (G_1 and τ). The last dashpot element (η) shows that the material viscosity for the Ca-alginate fiber is an order of magnitude higher than for the Mg-alginate fiber, as is seen in the slow creep of the Mg-alginate fiber which is largely absent from the Ca-alginate fiber. The Kelvin-Voigt model on its own works reasonably well to describe the behavior of the Ca-alginate fiber, as seen in Figure S3. However, due to the slow creep in the Mg-alginate

fiber, the Burgers model provides a better fit than Kelvin-Voigt (Figure S3).

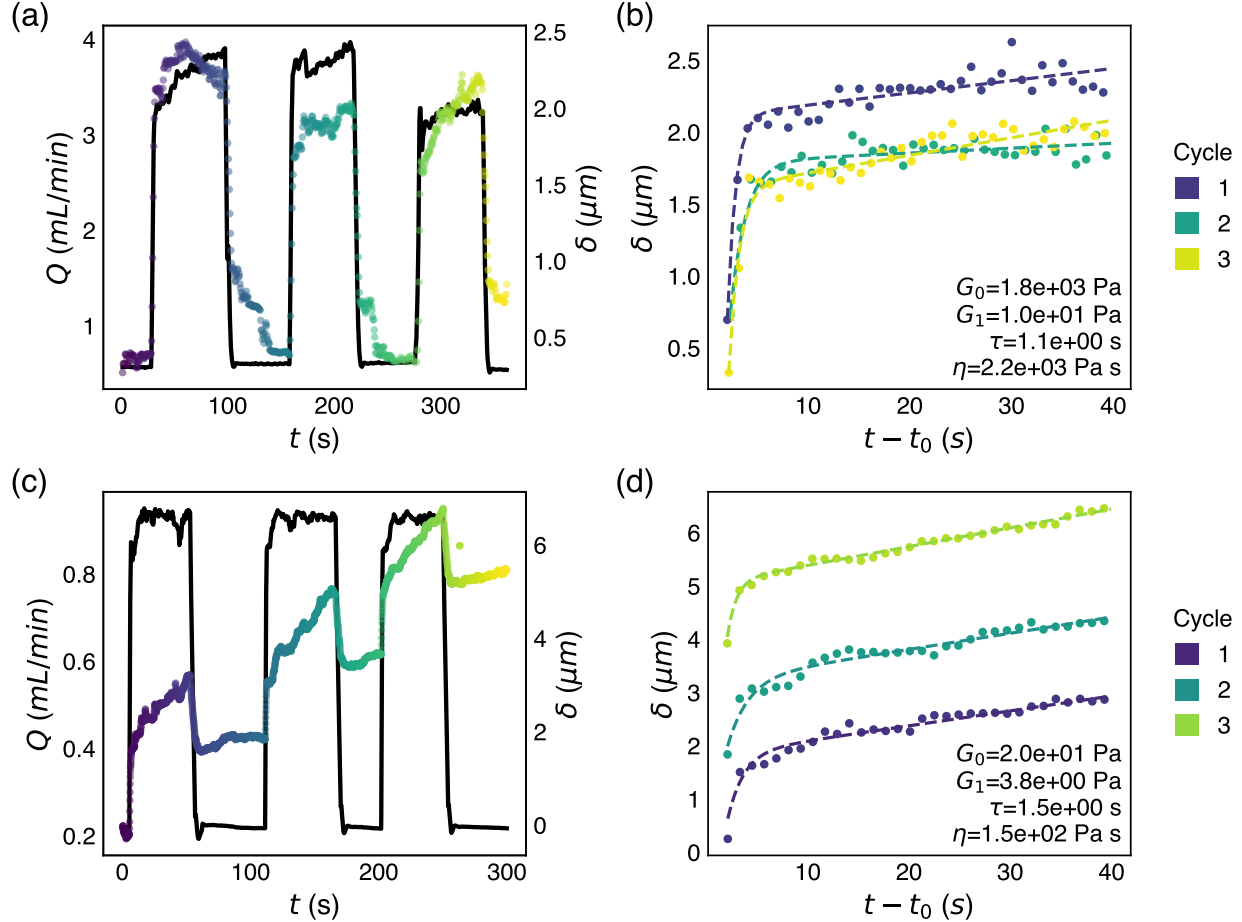


Figure 4: Cyclic loading reveals fiber creep. (a) The applied flow rate (black) and deflection (colored by time) of a Ca-alginate fiber during 3 square-wave loading cycles. (b) Creep data for the 3 loading cycles from (a) fitted with the Burgers model (dashed lines). The average fit parameters are listed in the lower right. (c) The applied flow rate (black) and deflection (colored by time) of a Mg-alginate fiber during a 3 square-wave loading cycle. (d) Creep data for the 3 loading cycles from (c) fitted with the Burgers model (dashed lines). The average fit parameters are listed in the lower right.

2. Dynamic Mechanical Analysis

An alternative way of exploring viscous behavior in a sample is using cyclic loading. On the macroscale, a technique called dynamic mechanical analysis (DMA) applies an oscillatory force on a material and measures the resulting deformation⁶¹. For viscoelastic samples, the

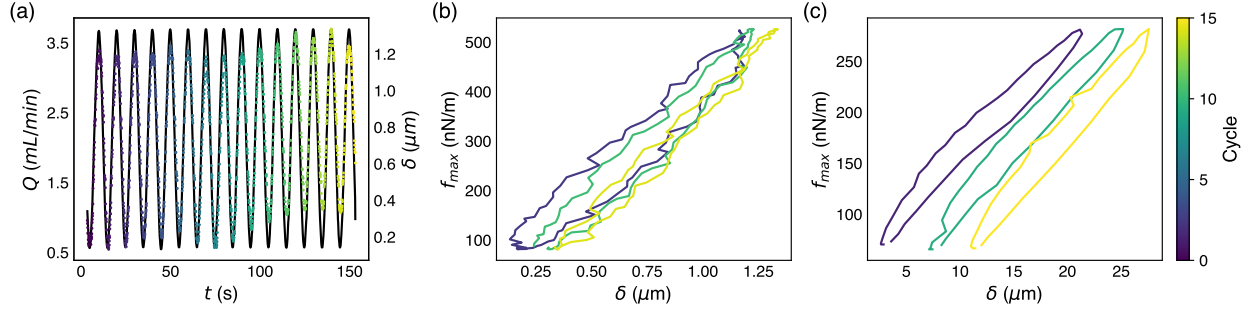


Figure 5: Cyclic loading reveals fiber properties. (a) An example of a sinusoidal cyclic loading test in a Ca-alginate fiber with 1% NaCl. Flow rate is plotted in black, deflection is plotted as a dotted line in black. (b) Comparison of the loading/unloading from the first and last cycles. The deflection increases slightly over the course of the experiment. (c) A similar test on a Mg-alginate Fiber shows a much larger creep in deflection.

deformation response is out of phase with the applied force, and the phase difference can be decomposed into an elastic and viscous component similarly to SAOS measurements performed on a rheometer.

Figure 5 demonstrates DMA tests at a frequency of 0.1 Hz performed on two different alginate fibers. Figure 5a shows the raw data of one such experiment on a Ca-alginate fiber. The color gradient line shows the flow rate oscillating between 600 and 3600 $\mu\text{L}/\text{min}$ 15 times over the course of 150 s, where the color gradient shows the time or cycle number. The dotted black line shows fiber deflection, which tracks closely with flow rate. The sine curves in Figure 5a, representing the applied stress and the material response, are offset by a phase angle ϕ . However, ϕ is small, and not very apparent by visual inspection of Figure 5a. Nonetheless we can fit both stimulus and response to sine curves in Figure 5a and obtain $\phi \sim 11^\circ$.

The phase offset between the flow rate and the deflection becomes more apparent in the Lissajous curves seen in Figure 5b. In large amplitude oscillatory shear (LAOS) measurements, Lissajous curves plot the oscillatory stress as a function of the oscillatory strain or strain rate. In the FIBR context, the oscillation of the applied hydrodynamic force causes an oscillation of the deflection, and plots of $\delta(f_{max})$ appear as closed loops. The plot shows the force and deflection measurements from three sinusoidal cycles at the beginning, middle, and end of the experiment in purple, green, and yellow colors respectively. Each of the curves shows the oval shape characteristic of a viscoelastic material. Over the course of

the experiment, the fiber shows slight net movement into the capillary of $\sim 0.2 \mu\text{m}$. Figure 5c shows the Lissajous curves of a similar cyclic loading experiment performed on a softer Mg-alginate fiber. This fiber demonstrates the same characteristic oval shape. However, the plastic deformation is much more significant in this sample, and the fiber moves nearly $10 \mu\text{m}$ into the capillary over the course of the experiment.

The curves in Figure 5b are less smooth than those in Figure 5c. This is largely due to the challenge of precisely determining the rod position below the light diffraction limit for the fiber in Figure 5b that bends $< 1 \mu\text{m}$, while the fiber in Figure 5c bends $20 \mu\text{m}$.

Lissajous plots provide the phase offset and the relative contribution of the storage and loss moduli to the signal. In LAOS, the volumetric energy stored during the measurement is proportional to an area of the curve: the change in applied stress multiplied by the change in strain. The area within the curves is proportional to the volumetric energy lost. The ratio of the loss modulus to the storage modulus is $\tan \phi$. The quantities obtained in FIBR are f_{\max} and δ . Converting to stress and strain requires dividing f_{\max} and δ by R and d , respectively. The dimensions of the area under the curve of $f_{\max}(\delta)$ are of force rather than modulus. However, the ratio of the two areas still provides $\tan \phi$. For the Ca-alginae and Mg-alginate samples shown in Figures 5b and 5c, $\phi = 11.8^\circ$ and $\phi = 10.3^\circ$, respectively. These values match closely the results from SAOS rheology, which give a phase angle of 9.4° and 7.8° for the Ca-alginate and Mg-alginate gels respectively as found via SAOS measurements.

3. Failure

In addition to time-dependent viscous measurements, the capillary bending technique can also measure other material characteristics, such as failure points. Figure 6 shows one example of buckling failure of a Mg-alginate fiber on a $200 \mu\text{m}$ capillary. Figure 6a shows the raw data from the experiment. Flow rate increases from 100 to $800 \mu\text{L}/\text{min}$ over the course of 100 s . This results in elastic-like deflection in the fiber up to $20 \mu\text{m}$. With this capillary, $> 800 \mu\text{L}/\text{min}$ is near the maximum possible flow rate and the flow rate is not as steady as we approach the limits of the vacuum pump. Nevertheless, as soon as the flow rate reaches $850 \mu\text{L}/\text{min}$, the fiber moves dramatically. Within a couple of seconds, the fiber deflection more than triples and a significant crease develops in the microscopy. Finally, the fiber folds in half and is pulled into the capillary. Given the measured flow rate at the onset of failure,

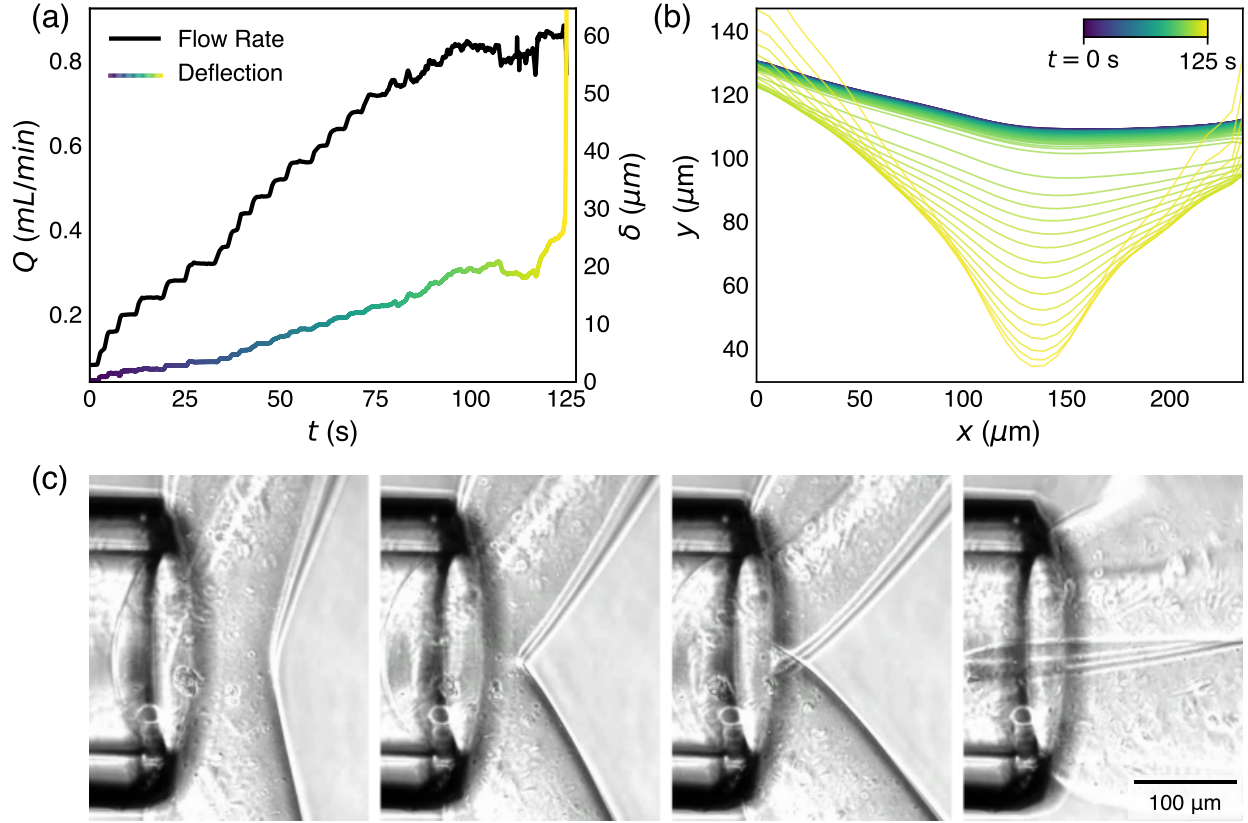


Figure 6: At a critical flow rate, the rod continues to deflect until it is pulled into the capillary, resulting in fiber failure. (a) Flow rate and deflection of a Mg-alginate fiber on a 200 μm capillary. Deflection increases rapidly at ~ 120 s once flow rate is set to ~ 850 $\mu\text{L}/\text{min}$. (b) Fitted contours show the shape change that rapidly happens at the end of the experiment. Color indicates the time: blue is $t = 0$ s, yellow is $t = 125$ s. (c) Microscopy showing the real-time rapid shape change of the Mg-alginate fiber during failure (Multimedia available online).

we estimate an applied stress ~ 120 Pa causes this sample to bend catastrophically. Notably for this sample, the fiber diameter is approximately the same size as the capillary so that significant squeezing must occur for the capillary to enter the capillary once folded in half. The video microscopy of this collapse, starting at $t = 124$ s and continuing to $t = 127$ s is seen in Figure 6c (Multimedia available online).

The range for measuring failure stress with the capillary aspiration setup is significantly narrower than the range for measuring the elastic modulus, due to the much larger bending that occurs during failure. While we can determine an elastic modulus with fiber movement

of $<5 \mu\text{m}$, fiber failure means significant deflection. Nevertheless, we still see failure modes in a range of materials. In addition to the Mg-alginate fiber in Figure 6, we have observed similar buckling failure in our alginate rods (cross-section $40 \times 25 \mu\text{m}$) measured on a $600 \mu\text{m}$ capillary. Young et al. report similar failure in some diatom samples, though do not discuss using this failure point as a means of characterizing samples²⁸.

C. Experimental Limits and Challenges

Parameter	Exp Min	Exp Max
δ	$1 \mu\text{m}$	$>100 \mu\text{m}$
d	$<2 \mu\text{m}$	$>300 \mu\text{m}$
L	$<200 \mu\text{m}$	$>2000 \mu\text{m}$
Q	$50 \mu\text{L}/\text{min}$	$15000 \mu\text{L}/\text{min}$
η	0.9 mPa s	0.9 mPa s

Table II: The range of parameters of the capillary bending technique as performed in this paper. The actual experimental limits may vary by up to an order of magnitude beyond what is done here.

Table II shows the range of parameters used in this study. Measurable deflection δ and fiber diameter d are limited by the diffraction limit in light microscopy. The upper limits for these will depend on the capillary size and the low strain assumption in the Euler beam theory. Glass capillaries can be bought at a variety of sizes and glass pulling can produce capillaries with internal diameters down to single micrometers. Additionally, the technique, in theory, should work for arbitrarily large sizes, although the pump and imaging requirements for diameters above several millimeters may require different equipment. The achievable flow rates will vary based on the size of the capillary and the capacity of the pump. Our Fluigent vacuum pump can achieve $\sim -900 \text{ mbar}$ of pressure. For the $600 \mu\text{m}$ capillary, this allows for flow rates up to $\sim 1 \text{ mL}/\text{min}$, while the $2000 \mu\text{m}$ capillary can draw $\sim 15 \text{ mL}/\text{min}$ at the same pressure. The lower flow rate limit depends on the resolution of

the pump and on the ability to hold the fiber in place. We use a low flow rate to hold the fiber in position against the capillary (50-500 $\mu\text{L}/\text{min}$ depending on the fiber size), although alternate methods for holding the fiber in position may allow for lower flow rates. Lastly, all experiments in this paper use water at room temperature, which has a viscosity of $\sim 0.9 \text{ mPa s}$. The experimental technique is not limited to this however, and adding solutes to the water, changing the solvent, and changing the temperature can all change the viscosity substantially.

With the experimental ranges given in Table II, we can measure flexural stiffnesses in the range $10^{-18} < EI < 10^{-12} \text{ Pa m}^4$. With differently sized capillaries and by varying other parameters as discussed above, one should be able to extend that range by at least an order of magnitude on either end. In Table I, we show the resulting elastic moduli ranging from 10^2 to 10^8 Pa . With sufficiently small fibers it may be possible to measure moduli several orders of magnitude higher. Consider the polyester fiber, which have a diameter of $28 \mu\text{m}$. A fiber with a similar effective stiffness but a diameter of $2.8 \mu\text{m}$ would have a modulus of $\sim 500 \text{ GPa}$. Softer fibers are also possible, although manipulating softer fibers may damage them. The $E = 300 \text{ Pa}$ Mg-alginate fibers are so soft that manipulating them with tweezers often collapses or breaks the fibers.

Within the experimental limits, we found the most common causes of error to be improper fiber alignment. Fibers must be positioned across the center of the capillary to properly quantify the span and ensure an appropriate force distribution. The fiber also must touch the capillary on both sides of the span. We rely on a low flow rate to pull the fiber onto the capillary, both to secure contact on both sides and position it on the longest span of the capillary. We have also found that longer fibers are more difficult to position in this way, and therefore harder to measure. Short fibers, $< 5 \times$ the capillary diameter, are able to be pulled into position more easily through the force of the flow alone. Longer fibers may require manual manipulation for positioning. Additionally, small manipulations at the loose end of a fiber can produce exaggerated movements down the length of the fiber. This is particularly a concern at high flow rates, as there may be substantial currents produced within the well by the water resupply line, which can dislodge the fiber from the capillary. Thus, choosing an appropriate capillary size and, if possible, reducing the length of the fiber will lead to easier and more accurate measurements.

V. CONCLUSION

The FIBR rheometer is uniquely capable of measuring small, soft, hydrated fibers. The technique is able to measure smaller and softer materials than traditional DMA instruments while avoiding the expense and difficulty in data analysis of an AFM. Simple elastic measurements with the capillary bending technique can be done very inexpensively with common equipment. While we use specialty pressure-driven pumps designed for microfluidics, any syringe pump with withdrawal capabilities is sufficient. For time-dependent measurements, changes in flow rate must be synchronized with the video recording; alternatively, tracer particles can be added to the water to determine flow rate via microscopy. More advanced dynamic mechanical analysis requires a pump configured to provide sinusoidal flow, and the range of accessible frequencies will depend on the pump's capabilities and flow rate resolution.

One limitation of the FIBR rheometer is that it controls for flow rate, and therefore stress, but not strain. Many applications, such as relaxation measurements, require achieving a specified strain. There may be an adaptation to the capillary bending rheometer which allows for controlling strain. With proper equipment and real-time image analysis, a feedback loop can adjust the stress in real time to achieve and maintain fiber deflection at a certain value. The delay inherent in any feedback loop likely limits this approach to equilibrium measurements and very low frequency oscillations.

The FIBR rheometer fills a critical gap for hydrated materials by operating in a submerged environment with non-destructive forces. This makes it particularly well-suited for biological materials and materials engineered for bio-environments, where maintaining hydration is essential for accurate characterization. Biological materials and cells, such as neurons, may be particularly amenable to measurement with this technique. Even beyond dynamic mechanical measurements, the hydrodynamic model and experimental setup can probe the active response of biological materials, that is, how living cells respond to forces in their environment. Many active and biological materials respond to external mechanical forcing by growing and/or adjusting their own material properties. FIBR could be adapted to measure such emergent states as a function of externally applied forces.

SUPPLEMENTAL MATERIAL

See the supplemental material for detailed hydrodynamic force calculations, comparison of exact and approximate analytical solutions, SAOS rheology data for bulk alginate gels, and alternative viscoelastic model fits for the creep data.

ACKNOWLEDGMENTS

BTS and SMH are supported by the NSF CBET CAREER 2239742 to SMH. The work of MC and ML was supported by the National Science Centre of Poland Sonata Bis grant no. 2023/50/E/ST3/00465 to ML.

We thank William Lee for his assistance in manufacturing and measuring alginate fibers.

CONFLICT OF INTEREST

The authors have no conflicts to declare.

DATA AVAILABILITY STATEMENT

The data that support the findings of this study are available from the corresponding author upon reasonable request.

REFERENCES

- ¹J. Du, Q. Ma, B. Wang, L. Sun, and L. Liu, “Hydrogel fibers for wearable sensors and soft actuators,” *iScience* **26**, 106796 (2023).
- ²L. Hertle, S. Sevim, J. Zhu, V. Pustovalov, A. Veciana, J. Llacer-Wintle, F. C. Landers, H. Ye, X.-Z. Chen, H. Vogler, U. Grossniklaus, J. Puigmartí-Luis, B. J. Nelson, and S. Pané, “A Naturally Inspired Extrusion-Based Microfluidic Approach for Manufacturing Tailorable Magnetic Soft Continuum Microrobotic Devices.” *Advanced materials (Deerfield Beach, Fla.)* **36** (2024), 10.1002/adma.202402309.

³W. Li, J. Wei, B. Li, J. Liu, Z. Yang, and C. Ren, “Recent Progress of Conductive Hydrogel Fibers for Flexible Electronics: Fabrications, Applications, and Perspectives,” *Advanced Functional Materials* **33**, 2213485 (2023).

⁴W. Xi, F. Kong, J. C. Yeo, L. Yu, S. Sonam, M. Dao, X. Gong, and C. T. Lim, “Soft tubular microfluidics for 2D and 3D applications,” *Proceedings of the National Academy of Sciences* **114**, 10590–10595 (2017).

⁵W. F. Heinz and J. H. Hoh, “Spatially resolved force spectroscopy of biological surfaces using the atomic force microscope,” *Trends in biotechnology* **17**, 143–150 (1999).

⁶R. Garcia, “Nanomechanical mapping of soft materials with the atomic force microscope: methods, theory and applications,” *Chemical Society Reviews* **49**, 5850–5884 (2020).

⁷M. Chyasnichyus, V. V. Tsukruk, and S. L. Young, “Recent advances in micromechanical characterization of polymer, biomaterial, and cell surfaces with atomic force microscopy,” *Japanese Journal of Applied Physics* **54**, 08LA02 (2015).

⁸V. G. Gisbert and R. Garcia, “Accurate Wide-Modulus-Range Nanomechanical Mapping of Ultrathin Interfaces with Bimodal Atomic Force Microscopy.” *ACS Nano* **15**, 20574–20581 (2021).

⁹T. Y. Tsui and G. M. Pharr, “Substrate effects on nanoindentation mechanical property measurement of soft films on hard substrates,” *Journal of Materials Research* **14**, 292–301 (1999).

¹⁰S. Vichare, S. Sen, and M. M. Inamdar, “Cellular mechanoadaptation to substrate mechanical properties: contributions of substrate stiffness and thickness to cell stiffness measurements using AFM,” *Soft Matter* **10**, 1174 (2013).

¹¹M. Asgari, M. Amabili, N. Latifi, H. D. Espinosa, and F. Giovanniello, “Revealing Layer-Specific Ultrastructure and Nanomechanics of Fibrillar Collagen in Human Aorta via Atomic Force Microscopy Testing: Implications on Tissue Mechanics at Macroscopic Scale,” *Advanced NanoBiomed Research* **2**, 2100159 (2022).

¹²C. J. G. Abrego, O. Deschaume, M. P. Lettinga, C. Bartic, J. Wellens, A. Vananroye, L. Dedroog, and J. Patterson, “Multiscale Characterization of the Mechanical Properties of Fibrin and Polyethylene Glycol (PEG) Hydrogels for Tissue Engineering Applications,” *Macromolecular Chemistry and Physics* **223**, 2100366 (2021).

¹³M. V. Flores-Merino, G. Battaglia, C. Lopresti, G. C. Reilly, S. Chirasatitsin, and A. J. Engler, “Nanoscopic mechanical anisotropy in hydrogel surfaces.” *Soft Matter* **6**, 4466

(2010).

¹⁴S. D. Solares, “Nanoscale effects in the characterization of viscoelastic materials with atomic force microscopy: coupling of a quasi-three-dimensional standard linear solid model with in-plane surface interactions,” *Beilstein Journal of Nanotechnology* **7**, 554–571 (2016).

¹⁵Y. Ding, G.-K. Xu, and G.-F. Wang, “On the determination of elastic moduli of cells by AFM based indentation,” *Scientific Reports* **7** (2017), 10.1038/srep45575.

¹⁶J. T. Pham, F. Schellenberger, H.-J. Butt, and M. Kappl, “From elasticity to capillarity in soft materials indentation,” *Physical Review Materials* **1** (2017), 10.1103/physrevmaterials.1.015602.

¹⁷D. He, D. Malu, and Y. Hu, “A Comprehensive Review of Indentation of Gels and Soft Biological Materials,” *Applied Mechanics Reviews* **76**, 1–59 (2024).

¹⁸W. Megone, J. E. Gautrot, and N. Roohpour, “Impact of surface adhesion and sample heterogeneity on the multiscale mechanical characterisation of soft biomaterials,” *Scientific Reports* **8** (2018), 10.1038/s41598-018-24671-x.

¹⁹P. F. Salipante, “Microfluidic techniques for mechanical measurements of biological samples,” *Biophysics Reviews* **4**, 011303 (2023).

²⁰R. M. Robertson-Anderson, “Optical tweezers microrheology maps micro-mechanics of complex systems,” *Trends in biochemical sciences* **49**, 649–650 (2024).

²¹F. Català-Castro, E. Schäffer, and M. Krieg, “Exploring cell and tissue mechanics with optical tweezers,” *Journal of Cell Science* **135**, jcs259355 (2022).

²²A. Amir, F. Babaeipour, D. B. McIntosh, D. R. Nelson, and S. Jun, “Bending forces plastically deform growing bacterial cell walls,” *Proceedings of the National Academy of Sciences* **111**, 5778–5783 (2014), publisher: Proceedings of the National Academy of Sciences.

²³C. Duprat, H. Berthet, J. S. Wexler, O. Du Roure, and A. Lindner, “Microfluidic in situ mechanical testing of photopolymerized gels,” *Lab on a Chip* **15**, 244–252 (2015).

²⁴A. Chakrabarti, S. Al-Mosleh, and L. Mahadevan, “Instabilities and patterns in a submerged jelling jet,” *Soft Matter* **17**, 9745–9754 (2021), publisher: The Royal Society of Chemistry.

²⁵T. Aoki, T. Ohashi, T. Matsumoto, and M. Sato, “The pipette aspiration applied to the local stiffness measurement of soft tissues,” *Annals of Biomedical Engineering* **25**, 581–587 (1997).

²⁶M. Guo and H. M. Wyss, “Micromechanics of Soft Particles,” *Soft Matter* **6**, 4550–4555 (2010).

²⁷H. M. Wyss, T. Franke, E. Mele, and D. A. Weitz, “Capillary micromechanics: Measuring the elasticity of microscopic soft objects,” *Soft Matter* **6**, 4550–4555 (2010), publisher: Royal Society of Chemistry.

²⁸A. M. Young, L. Karp-Boss, P. A. Jumars, and E. N. Landis, “Quantifying diatom aspirations: Mechanical properties of chain-forming species,” *Limnology and Oceanography* **57**, 1789–1801 (2012).

²⁹M. Zhou, J. Gong, and J. Ma, “Continuous fabrication of near-infrared light responsive bilayer hydrogel fibers based on microfluidic spinning,” *e-Polymers* **19**, 215–224 (2019).

³⁰T. R. Cuadros, O. Skurys, and J. M. Aguilera, “Mechanical properties of calcium alginate fibers produced with a microfluidic device,” *Carbohydrate Polymers* **89**, 1198–1206 (2012).

³¹F. Topuz, A. Henke, W. Richtering, and J. Groll, “Magnesium ions and alginate do form hydrogels: a rheological study,” *Soft Matter* **8**, 4877 (2012).

³²M. A. LeRoux, F. Guilak, and L. A. Setton, “Compressive and shear properties of alginate gel: Effects of sodium ions and alginate concentration,” *Journal of Biomedical Materials Research* **47**, 46–53 (1999).

³³B. T. Smith and S. M. Hashmi, “In situ polymer gelation in confined flow controls intermittent dynamics,” *Soft Matter* **20**, 1858–1868 (2024), publisher: Royal Society of Chemistry.

³⁴B. T. Smith and S. M. Hashmi, “Diffusion-driven deposition model suggests stiffer gels deposit more efficiently in microchannel flows,” *Physics of Fluids* **36** (2024).

³⁵P. Agulhon, M. Robitzer, J.-P. Habas, and F. Quignard, “Influence of both cation and alginate nature on the rheological behavior of transition metal alginate gels,” *Carbohydrate Polymers* **112**, 525–531 (2014).

³⁶S. van der Walt, J. L. Schönberger, J. Nunez-Iglesias, F. Boulogne, J. D. Warner, N. Yager, E. Gouillart, T. Yu, and t. s.-i. contributors, “scikit-image: image processing in Python,” *PeerJ* **2**, e453 (2014).

³⁷J. Rotne and S. Prager, “Variational treatment of hydrodynamic interaction in polymers,” *The Journal of Chemical Physics* **50**, 4831–4837 (1969).

³⁸H. Yamakawa, “Transport properties of polymer chains in dilute solution: hydrodynamic interaction,” *The Journal of Chemical Physics* **53**, 436–443 (1970).

³⁹P. J. Zuk, E. Wajnryb, K. Mizerski, and P. Szymczak, “Rotne–prager–yamakawa approximation for different-sized particles in application to macromolecular bead models,” *Journal of Fluid Mechanics* **741**, R5 (2014).

⁴⁰O. A. Bauchau and J. I. Craig, *Structural analysis: with applications to aerospace structures*, Vol. 163 (Springer Science & Business Media, 2009).

⁴¹F. M. White, “Fluid mechanics,” (1999).

⁴²J. Gray and G. J. Hancock, “The propulsion of sea-urchin spermatozoa,” *Journal of Experimental Biology* **32**, 802–814 (1955).

⁴³R. Johnson and C. Brokaw, “Flagellar hydrodynamics. a comparison between resistive-force theory and slender-body theory,” *Biophysical journal* **25**, 113–127 (1979).

⁴⁴J. K. Dhont, *An introduction to dynamics of colloids*, Vol. 2 (Elsevier, 1996).

⁴⁵R. H. C. Bonser and P. P. Purslow, “The Young’s Modulus of Feather Keratin,” *Journal of Experimental Biology* **198**, 1029–1033 (1995).

⁴⁶R. H. C. Bonser and J. Farrent, “Influence of hydration on the mechanical performance of duck down feathers,” *British Poultry Science* **42**, 271–273 (2001).

⁴⁷N. Reddy and Y. Yang, “Structure and Properties of Chicken Feather Barbs as Natural Protein Fibers,” *Journal of Polymers and the Environment* **15**, 81–87 (2007).

⁴⁸M. E. Fuller, *The structure and properties of down feathers and their use in the outdoor industry, phd*, University of Leeds (2015).

⁴⁹O. A. Plushchik and A. N. Aniskevich, “Effects of temperature and moisture on the mechanical properties of polyester resin in tension,” *Mechanics of Composite Materials* **36**, 233–240 (2000).

⁵⁰A. N. Fraga, V. A. Alvarez, A. Vazquez, and O. de la Osa, “Relationship between Dynamic Mechanical Properties and Water Absorption of Unsaturated Polyester and Vinyl Ester Glass Fiber Composites,” *Journal of Composite Materials* **37**, 1553–1574 (2003), publisher: SAGE Publications Ltd STM.

⁵¹H. Shirataki, A. Nakashima, K. Sato, and K. Okajima, “Correlation between tensile properties and network draw ratio for poly(ethylene terephthalate) fibers with wide range of molecular orientation and crystallinity,” *Journal of Applied Polymer Science* **64**, 2631–2646 (1997).

⁵²E. Karaca and F. Ozcelik, “Influence of the cross-sectional shape on the structure and properties of polyester fibers,” *Journal of Applied Polymer Science* **103**, 2615–2621 (2007).

⁵³H. Malektaj, A. D. Drozdov, J. d. Christiansen, H. Malektaj, A. D. Drozdov, and J. d. Christiansen, “Mechanical Properties of Alginate Hydrogels Cross-Linked with Multivalent Cations,” *Polymers* **15** (2023), 10.3390/polym15143012, company: Multidisciplinary Digital Publishing Institute Distributor: Multidisciplinary Digital Publishing Institute Institution: Multidisciplinary Digital Publishing Institute Label: Multidisciplinary Digital Publishing Institute Publisher: publisher.

⁵⁴B. E. Larsen, J. Bjørnstad, E. O. Pettersen, H. H. Tønnesen, and J. E. Melvik, “Rheological characterization of an injectable alginate gel system,” *BMC Biotechnology* **15**, 29 (2015).

⁵⁵S. Zhang, X. Liu, S. F. Barreto-Ortiz, Y. Yu, B. Ginn, N. DeSantis, D. L. Hutton, W. Grayson, F.-Z. Cui, B. A. Korgel, S. Gerecht, and H.-Q. Mao, “Creating Polymer Hydrogel Microfibres with Internal Alignment via Electrical and Mechanical Stretching,” *Biomaterials* **35**, 3243–3251 (2014).

⁵⁶J. Su, Y. Zheng, and H. Wu, “Generation of alginate microfibers with a roller-assisted microfluidic system,” *Lab on a Chip* **9**, 996–1001 (2009), publisher: The Royal Society of Chemistry.

⁵⁷D. Roylance, “ENGINEERING VISCOELASTICITY,” Department of Materials Science and Engineering-Massachusetts Institute of Technology , 1–37 (2001).

⁵⁸R. S. Lakes, *Viscoelastic Solids* (1998) (CRC Press, Boca Raton, 2017).

⁵⁹A. Y. Malkin and A. I. Isayev, *Rheology: Concepts, Methods, and Applications* (Elsevier, 2022).

⁶⁰J. Li, H. Liu, C. Wang, and G. Huang, “A facile method to fabricate hybrid hydrogels with mechanical toughness using a novel multifunctional cross-linker,” *RSC Advances* **7**, 35311–35319 (2017).

⁶¹K. P. Menard and N. Menard, *Dynamic Mechanical Analysis*, 3rd ed. (CRC Press, Boca Raton, 2020).

⁶²S. Kim and S. J. Karrila, *Microhydrodynamics: principles and selected applications* (Butterworth-Heinemann, 2013).

⁶³M. Manghi, X. Schlagberger, Y.-W. Kim, and R. R. Netz, “Hydrodynamic effects in driven soft matter,” *Soft Matter* **2**, 653–668 (2006).

⁶⁴C. M. Wang, H. Zhang, N. Challamel, and W. Pan, *Hencky bar-chain/net for structural analysis* (World Scientific, 2020).

VI. SUPPLEMENTAL INFORMATION

A. Calculations of the hydrodynamic load on the fibers

For microscale objects, the flow \mathbf{u} around the whole fluid domain is governed by the incompressible Stokes equations

$$\eta \nabla^2 \mathbf{u} - \nabla p + \mathbf{f} = 0, \quad (\text{S1})$$

$$\nabla \cdot \mathbf{u} = 0, \quad (\text{S2})$$

where η is the dynamic viscosity and p is the pressure field. If a force \mathbf{F} acts on a particle immersed in Stokes flow, it will move with a velocity \mathbf{u} according to the relationship

$$\mathbf{u} = \boldsymbol{\mu} \cdot \mathbf{F}, \quad (\text{S3})$$

where $\boldsymbol{\mu}$ is the mobility matrix⁶². The linear relationship also holds for a multiparticle system, where for N particles the vectors \mathbf{u} and \mathbf{F} take the form of $\mathbf{u} = [\mathbf{u}_1, \dots, \mathbf{u}_N]$ and $\mathbf{F} = [\mathbf{F}_1, \dots, \mathbf{F}_N]$, and $\boldsymbol{\mu}$ is a $3N \times 3N$ matrix composed of 3×3 blocks $\boldsymbol{\mu}_{ij}$. A sub-matrix $\boldsymbol{\mu}_{ij}$ relates the velocity of particle i to the forces acting on particle j . In Stokesian Dynamics, and in the absence of ambient flow, the configuration of the system $\mathbf{R} = [\mathbf{R}_1, \dots, \mathbf{R}_N]$ evolves according to

$$\frac{d\mathbf{R}}{dt} = \boldsymbol{\mu} \cdot \mathbf{F}. \quad (\text{S4})$$

In general, the mobility matrix $\boldsymbol{\mu}$ depends on the positions of all particles. Assuming that the particles interacting in the fluid are identical spheres of radius a , we shall use the pairwise Rotne-Prager-Yamakawa approximation to resolve the hydrodynamic interactions. Within this model, we assume that $\boldsymbol{\mu}_{ij}$ depends only on the positions of the particles i and j via

$$\frac{\boldsymbol{\mu}_{ij}}{\mu_0} = \begin{cases} \frac{3a}{4R_{ij}} \left[\left(1 + \frac{a^2}{3R_{ij}^2}\right) \mathbf{1} + \left(1 - \frac{2a^2}{R_{ij}^2}\right) \hat{\mathbf{R}}_{ij} \hat{\mathbf{R}}_{ij} \right] & \text{for } R_{ij} \geq 2a, \\ \left(1 - \frac{9R_{ij}}{32a}\right) \mathbf{1} + \frac{3R_{ij}}{32a} \hat{\mathbf{R}}_{ij} \hat{\mathbf{R}}_{ij} & \text{for } 2a \geq R_{ij} > 0, \end{cases} \quad (\text{S5})$$

where a_i denotes the radius of the i -th bead, $R_{ij} = |\mathbf{R}_{ij}|$ is the distance between the i -th and j -th bead, and $\hat{\mathbf{R}}_{ij}$ is the unit vector from bead i to bead j . Here, $\mu_0 = (6\pi\eta a)^{-1}$ is the Stokesian mobility of an isolated spherical particle. Within this approximation, the velocity of the sphere i , $\mathbf{U}_i = d\mathbf{R}_i/dt$, is given by

$$\mathbf{U}_i = \sum_j \boldsymbol{\mu}_{ij} \cdot \mathbf{F}_j = \mu_0 \mathbf{F}_i + \sum_{j \neq i} \boldsymbol{\mu}_{ij} \cdot \mathbf{F}_j, \quad (\text{S6})$$

where we singled out the self-term $i = j$ being the Stokes velocity.

We now introduce the bead-model, in which a fiber is represented by a collection of $2N+1$ identical, possibly overlapping spheres, located at the points \mathbf{R}_i , with $i = 1, \dots, 2N+1$, initially aligned together in the form of a straight rod^{63,64}. The diameter of each bead is $2a$, and the centers of the subsequent beads are separated by a distance l_0 .

The experiments span a range of aspect ratios. We distinguish two regimes by comparing the diameter of the fiber, $d = 2a$, to the diameter of the capillary. This aspect ratio R/d , determines whether the fiber is ‘thick’ or ‘thin’. We model these limits differently: for thick fibers we assume that the capillary diameter is filled with overlapping beads, while for thin fibers we represent the fiber by a string of non-overlapping and touching beads.

The idea behind the calculation is the following. Because in the initial state the flow is perpendicular to the vector $\hat{\mathbf{R}}_{ij}$, for every ij pair the dyadic part of the mobility matrix does not contribute to the final expression. For the perpendicular direction, along the axis of the capillary z , we can write down

$$U_i^z = \mu_{ij}^{zz} F_j^z \quad (\text{S7})$$

Initially, thin filaments are considered. The thin filament is modeled as a collection of $2N+1$ spherical beads of radius a , such that the centers of the outermost beads are located at positions $x = \pm R$. The beads are arranged so that each one touches only its immediate neighbors, and the contacts occur at a single point. In such geometry, the zz components of the mobility matrix take the form of

$$\mu_{ij}^{zz} = \begin{cases} \frac{1}{16\pi\eta a|i-j|} \left(1 + \frac{1}{6|i-j|^2}\right) & \text{for } i \neq j, \\ \frac{1}{6\pi\eta a} & \text{for } i = j. \end{cases} \quad (\text{S8})$$

The main focus is the velocity felt by the middle bead ($i = N+1$) and the total force acting on the middle bead. Using equations (S8) and (3), we find

$$\begin{aligned} U_{\max} &= \sum_{i=1}^{2N+1} \mu_{Nj}^{zz} F_j = \\ &= \frac{F_{\max}}{16\pi\eta a} \sum_{i \neq N}^{2N+1} \left(\frac{1}{|i-N|} + \frac{1}{6|i-N|^3} - \frac{|i-N|^3}{N^4} - \frac{|i-N|}{6N^4} \right) + \\ &+ \frac{F_{\max}}{6\pi\eta a} = \frac{F_{\max}}{8\pi\eta a} \sum_{k=1}^N \left(\frac{1}{k} + \frac{1}{6k^3} - \frac{k^3}{N^4} - \frac{k}{6N^4} \right) + \frac{F_{\max}}{6\pi\eta a}. \end{aligned} \quad (\text{S9})$$

The exact analytical result of the above sum is given by:

$$F_{\max} = \frac{8\pi\eta a U_{\max}}{H_N + \frac{1}{6}H_N^{(3)} + \frac{13}{12} - \frac{1}{2N} - \frac{1}{3N^2} - \frac{1}{12N^3}}. \quad (\text{S10})$$

where H_n and $H_n^{(3)}$ denote the harmonic numbers and the harmonic numbers of the second order, respectively.

For sufficiently large N , and therefore large aspect ratio k , we can simplify Eq. (S10) and divide by the characteristic length $l_0 = 2a$ to obtain equation (7). The approximate solution in equation (7) provides f_{\max} , a force per unit length. To compare the exact analytical result in Eq. (S10) to Eq. (7), we also divide F_{\max} by l_0

$$f_{\max} = \frac{4\pi\eta U_{\max}}{H_N + \frac{1}{6}H_N^{(3)} + \frac{13}{12} - \frac{1}{2N} - \frac{1}{3N^2} - \frac{1}{12N^3}}. \quad (\text{S11})$$

The differences between the forces calculated using the exact and approximate solutions are small, as shown in Figure S1. Therefore, the approximate version is used to interpret experimental measurements.

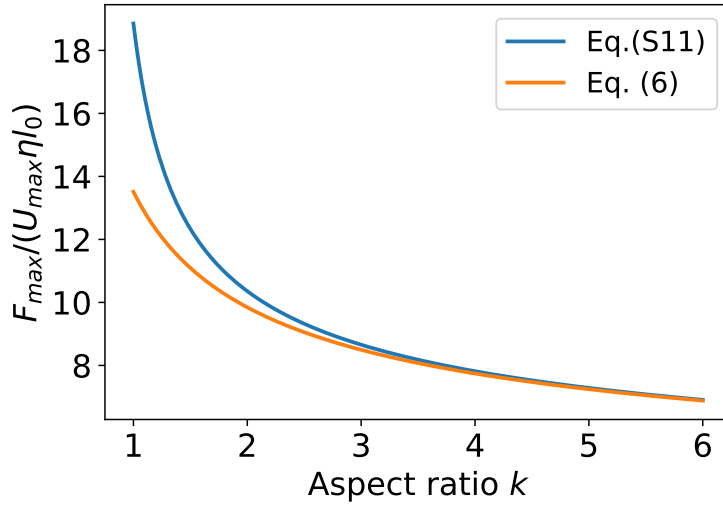


Figure S1: Comparison of the dimensionless force values obtained from the exact (Eq. (S10)) and approximate (Eq. (7)) solutions. We observe that the differences are generally small and decrease as the aspect ratio k increases.

In the case of thick filaments we proceed differently. Let us assume that the ratio of the tube radius R to the sphere radius a is equal to k , where $k \in [1, 2]$. We then construct a

filament from $2N + 1$ overlapping beads such that the centers of the outermost beads are located at positions $x = \pm R$, and the distance between two neighboring beads is $R_{i,i+1} = ka/N$. The zz components of the mobility matrix take the form³⁹

$$\mu_{ij}^{zz} = \begin{cases} \frac{1}{6\pi\eta a} \left(1 - \frac{9k|i-j|}{32N} \right) & \text{for } i \neq j, \\ \frac{1}{6\pi\eta a} & \text{for } i = j. \end{cases} \quad (\text{S12})$$

Instead of force acting on the middle bead, we will focus on the force acting on the part of the middle bead of length ka/N :

$$\begin{aligned} U_{\max} &= \sum_{i=1}^{2N+1} \mu_{Nj}^{zz} F_j = \\ &= \frac{f_{\max}}{6\pi\eta a} \sum_{i \neq N}^{2N+1} \left(1 - \frac{9|i-N|}{32N} - \frac{|i-N|^4}{N^4} + \frac{9|i-N|^5}{32N^5} \right) + \frac{1}{6\pi\eta a} = \\ &= \frac{f_{\max}}{3\pi\eta a} \sum_{l=1}^N \left(1 - \frac{9kl}{32N} - \frac{l^4}{N^4} + \frac{9kl^5}{32N^5} \right) + \frac{F_0}{6\pi\eta a}. \end{aligned} \quad (\text{S13})$$

Because the parameter N is arbitrary here, we will assume that $N \ll 1$, and therefore we can write down approximated relationship given by Eq. (8).

Force profiles found in both regimes were placed in Eq. (4) and integrated considering boundary conditions given by Eq. (5). The integration leads to the relationship in Eq. (6). By substituting the appropriate linear force densities and the corresponding second moments of area, we obtain expressions for E in both the thin and thick regimes, and for both cylindrical and square cross-sections. These expressions are given in equations (9)-(12). Substituting the exact expression for the linear force density for thin fibers from Eq. (S10) yields the following relation:

$$E = \frac{\eta U_{\max}}{\delta} \frac{192}{5} \frac{k^4}{H_k + \frac{1}{6} H_k^{(3)} + \frac{13}{12} - \frac{1}{2k} - \frac{1}{3k^2} - \frac{1}{1k^3}}. \quad (\text{S14})$$

B. Bulk Rheology

Figure S2 shows the small amplitude oscillatory shear rheology of two alginate gels prepared in bulk, after being soaked in calcium and magnesium salt baths. Figure S2a shows

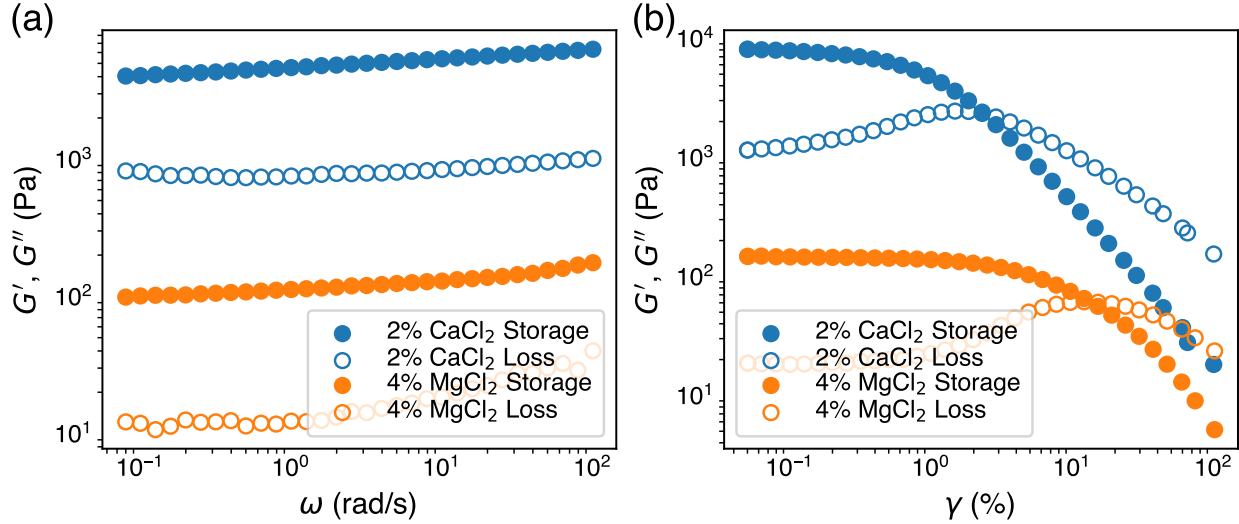


Figure S2: Small amplitude oscillatory shear rheology on bulk alginate gels.

a frequency sweep at a constant strain of 0.1%. Figure S2b shows an amplitude sweep at a frequency of 5 rad/s. The average moduli across the entire frequency sweep of Figure S2a are reported in the SAOS measurements in Table I.

C. Alternate Creep Models

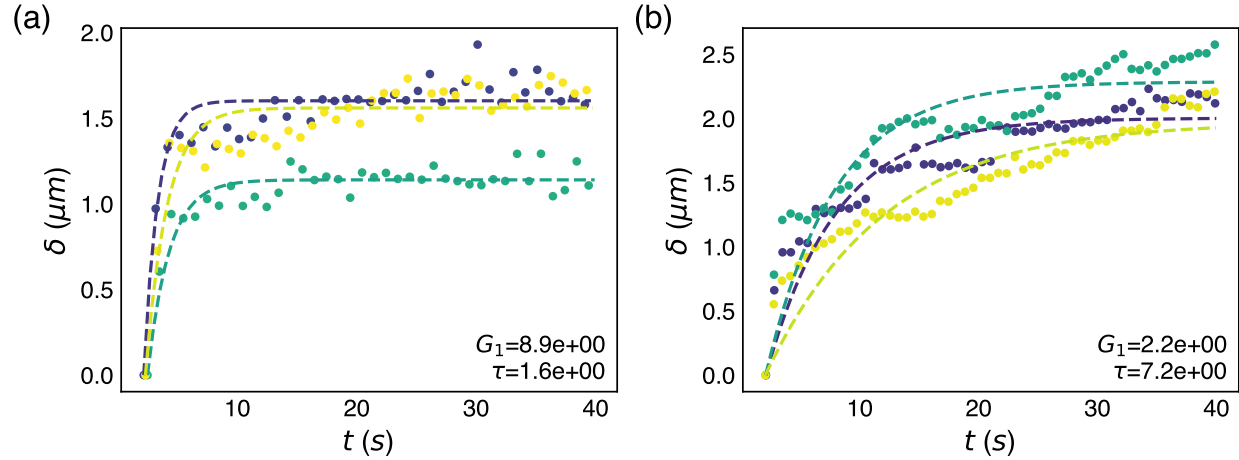


Figure S3: Kelvin-Voigt Fit to creep data.

Figures S3a and S3b show the creep data from Figures 4a for a Ca-alginate sample, and 4c for an Mg-alginate sample, respectively, as well as the fit of the Kelvin-Voigt model of

viscoelasticity^{59,60}. The Kelvin-Voigt model behaves according to the following equation:

$$J(t) = \frac{1}{G_1} (1 - e^{-t/\tau})$$

where J is the viscoelastic compliance $\gamma(t)/\sigma_0$, G_1 is the shear modulus of the spring element in the model and τ is the decay time.